

Towards Real Zero-Shot Camouflaged Object Segmentation without Camouflaged Annotations

Cheng Lei, Jie Fan, Xinran Li, Tianzhu Xiang, Ao Li, Ce Zhu, Le Zhang

Abstract—Camouflaged Object Segmentation (COS) faces significant challenges due to the scarcity of annotated data, where meticulous pixel-level annotation is both labor-intensive and costly, primarily due to the intricate object-background boundaries. Addressing the core question, "Can COS be effectively achieved in a zero-shot manner without manual annotations for any camouflaged object?" we affirmatively respond and introduce a robust zero-shot COS framework. This framework leverages the inherent local pattern bias of COS and employs a broad semantic feature space derived from salient object segmentation (SOS) for efficient zero-shot transfer. We incorporate an Masked Image Modeling (MIM) based image encoder optimized for Parameter-Efficient Fine-Tuning (PEFT), a Multimodal Large Language Model (M-LLM), and a Multi-scale Fine-grained Alignment (MFA) mechanism. The MIM pre-trained image encoder focuses on capturing essential low-level features, while the M-LLM generates caption embeddings processed alongside these visual cues. These embeddings are precisely aligned using MFA, enabling our framework to accurately interpret and navigate complex semantic contexts. To optimize operational efficiency, we introduce a learnable codebook that represents the M-LLM during inference, significantly reducing computational overhead. Our framework demonstrates its versatility and efficacy through rigorous experimentation, achieving state-of-the-art performance in zero-shot COS with F_{β}^w scores of 72.9% on CAMO and 71.7% on COD10K. By removing the M-LLM during inference, we achieve an inference speed comparable to that of traditional end-to-end models, reaching 18.1 FPS. Additionally, our method excels in polyp segmentation, outperforming challenging baselines in both zero-shot and supervised settings, thereby highlighting its potential for broad applicability in diverse segmentation tasks.

Index Terms—Camouflaged Object Segmentation, Zero-Shot, Fine-Tuning

1 INTRODUCTION

Camouflaged Object Segmentation (COS) is an emerging computer vision task focused on accurately segmenting objects that seamlessly blend into their surrounding environments [1], [2]. Unlike existing segmentation tasks such as salient object segmentation (SOS), where segmented objects are distinctly different from the background and each other, as illustrated in the rows of Fig. 1, COS presents a significant challenge due to the inherent visual similarity between foreground objects and the background. This similarity makes it difficult to identify distinguishing cues for accurate separation. Existing COS methods often rely heavily on large-scale annotated datasets. However, creating and accessing such datasets pose significant challenges, primarily due to the demanding nature of extensive pixel-level annotations, which are both time-consuming and labor-intensive [3], [4].

Efforts to mitigate these challenges have led to the development of weakly-supervised methods utilizing scribbles or points, aiming to reduce annotation time [4], [5]. However, these methods remain time-consuming, especially when dealing with large-scale datasets. In such contexts, zero-shot learning emerges as a crucial approach, eliminating the need for explicit data labeling for downstream tasks.

Existing methodologies such as zero-shot camouflaged object detection (ZSCOD) [6] and open-vocabulary camouflaged object segmentation (OVCOS) [7] focus on identifying specific classes of objects, aiming to segment unseen classes

as depicted in Fig. 2. However, both ZSCOD and OVCOS still require partial data labeling from the COS dataset for training, which does not fully eliminate the need for explicit annotations [6], [7]. This limitation highlights the importance of developing a more pragmatic, real-world approach to zero-shot camouflaged object segmentation (ZSCOS) that minimizes reliance on the COS dataset.

Recent developments by GenSAM [8] and MMCPF [9] have made strides in addressing these issues by employing prompt engineering to synergize SAM [10] with M-LLM for ZSCOS. These methods effectively utilize the capabilities of pre-trained models and circumvent the necessity for extensive post-training, thereby streamlining the deployment process. However, they continue to encounter substantial computational overhead during inference, which may limit their practical applicability in resource-constrained settings. This underscores the need for further exploration into solutions that are both efficient and effective, aiming to fully address the constraints of existing methodologies.

Recall that our zero-shot COS task is inherently a zero-shot dense prediction problem. In zero-shot learning, recent studies have shown that the ability to extract robust semantic features is crucial for success [11]. On the other hand, for dense prediction tasks, effectively processing high-frequency details is essential to accurately capture fine object boundaries [12]. This dual challenge has led us to hypothesize that combining a training dataset rich in semantic information with a pre-trained model proficient in dense prediction could significantly benefit our zero-shot COS approach. By doing so, the system not only improves its ability to capture high-frequency details, essential for object boundary delineation, but also enhances its understanding

C. Lei, J. Fan, X. Li, A. Li, C. Zhu and L. Zhang are with University of Electronic Science and Technology of China.

T.-Z. Xiang is with the Inception Institute of Artificial Intelligence and G42, UAE.

C. Lei and J. Fan contribute equally and L. Zhang is the corresponding author.

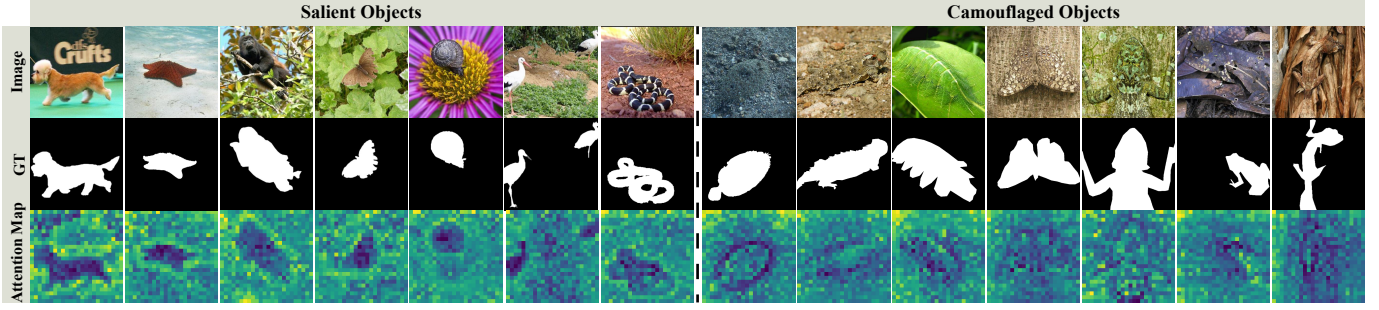


Fig. 1. **Examples of salient and camouflaged objects.** In salient object segmentation (SOS), objects are easily distinguishable from the background, while in camouflaged object segmentation (COS), objects blend into their surroundings. The attention maps reveal that SOS focuses on semantic information, whereas COS emphasizes edge features to detect camouflaged objects.

of semantic features, which are critical for zero-shot learning in dense prediction contexts.

Further empirical observations, illustrated in Fig. 1, offer additional insights for COS. Specifically, we extract the attention map from the final transformer block of the image encoder, which provides a two-dimensional visualization of the attention weights. These weights are computed by the dot product between the query matrix and the corresponding value matrix, and subsequently averaged across all attention heads. The analysis reveals that while SOS models primarily focus on low-frequency features within semantically significant areas, COS models excel in identifying high-frequency features critical for outlining the edges of camouflaged objects. This difference underscores the value of integrating an SOS dataset into our training approach. Using SOS datasets not only exploits their rich semantic content, beneficial for enhancing COS, but also takes advantage of their wider availability, cost-effectiveness, and the extensive existing research on them.

With this strategy in mind, as depicted in Fig. 2, our image encoder, initially pre-trained using Masked Image Modeling (MIM) [12], undergoes further refinement through a SOS dataset. The training data from SOS significantly contributes to this phase by emphasizing discernible semantic contrasts through fine-grained alignment. Simultaneously, the MIM’s inherent strength in capturing high-frequency details is leveraged to enhance the model’s precision in identifying minute and intricate object boundaries. This training regimen not only broadens the model’s perceptual scope but also sharpens its detail resolution, establishing a robust foundation for handling complex visual segmentation tasks.

Building on the success reported in [13], we further incorporate Multimodal Large Language Models (M-LLM) to provide captions for fine-grained alignment, optimizing the model to capture intricate semantic features essential for dense prediction tasks. During training, the MIM pre-trained image encoder generates visual embeddings that capture low-level features, while the M-LLM processes task-specific prompts alongside the image to produce corresponding caption embeddings. These embeddings are carefully aligned within our framework, enabling the model to effectively leverage the rich semantic content from the M-LLM and align it with the visual features. Such synchronized understanding is vital for the model to accurately interpret complex semantic contexts, thus enhancing its ability

to perform tasks that require a profound understanding of inputs. During inference, the M-LLM is deactivated, and instead, a query learned during training serves as a codebook, replacing the caption embeddings and working alongside the visual embeddings to generate accurate masks.

To summarize, in this work we address a significant question: Is it possible to achieve zero-shot camouflaged object segmentation (COS) without manual annotations for any camouflaged object? And our contributions are as follows:

- We affirmatively answer the question of zero-shot COS feasibility and introduce a new framework that supports both zero-shot and supervised learning modes for COS. This framework efficiently integrates vision and caption embeddings, utilizing a novel feature fusion module that optimizes semantic alignment and enhances model performance. This also helps us to establish a foundational link between camouflaged object segmentation and salient object segmentation, demonstrating the beneficial interaction between these two tasks for enhancing COS.
- We further develop a method for training a codebook that substitutes the need for Multimodal Large Language Models (M-LLM) during inference, significantly reducing the computational overhead and enabling more efficient deployment.
- Our approach sets new benchmarks in zero-shot camouflaged object segmentation, delivering performance on par with existing weakly-supervised methods. Furthermore, it shows robust competitiveness in supervised COS scenarios. Moreover, our method significantly outperforms challenging baselines in polyp segmentation in both zero-shot and supervised settings, showcasing its broad applicability and effectiveness across a variety of segmentation tasks.

2 RELATED WORK

2.1 Camouflaged Object Segmentation

COS is a recently emerging computer vision task, that has garnered increasing attention from the community. To accurately localize and segment camouflaged objects, numerous deep learning-based methods have been proposed, which can be roughly divided into supervised methods and

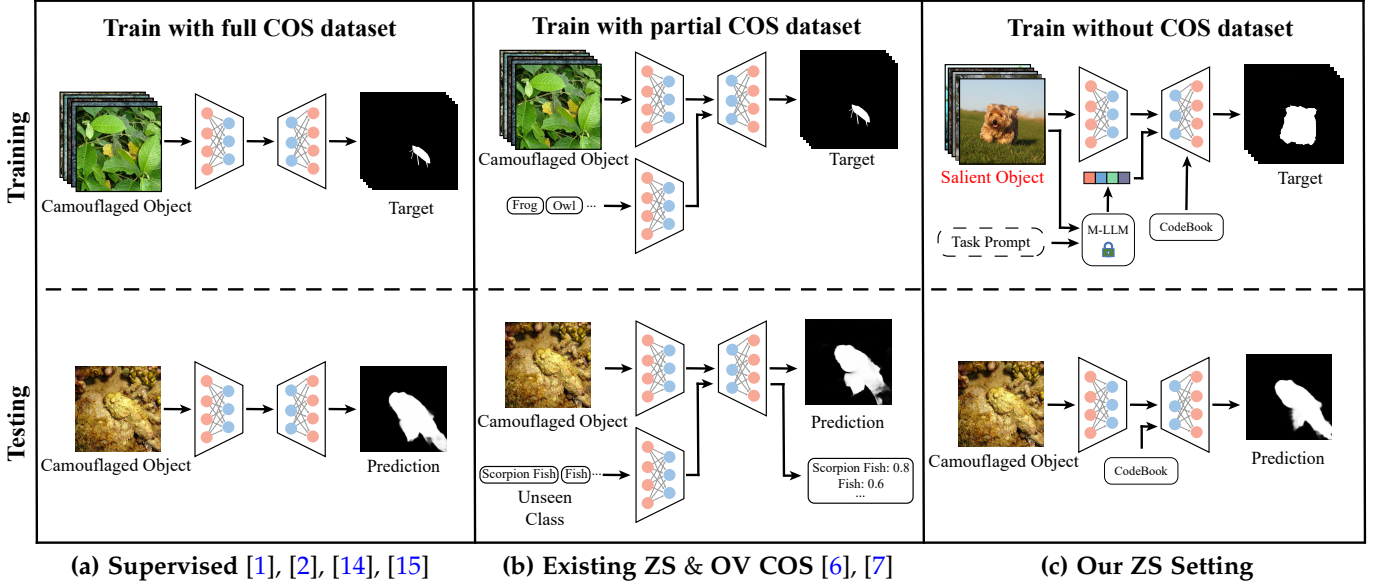


Fig. 2. Overview of different learning pipeline to COS. In Supervised COS (a), camouflaged objects are used for both training and testing [1], [2], [14], [15]. In Zero-Shot COD [6] & Open-Vocabulary [7] (b), training data consists of a specific set of camouflaged objects, while testing data includes unseen camouflaged objects. Our Zero-shot COS (c) setting offers a more practical approach as it is trained without any camouflaged annotations. Instead, we utilize a saliency dataset, which is more readily available, cost-effective.

weakly-supervised methods. The former often rely on large-scale pixel-level annotated data sets, including bio-inspired methods [1], [2], multi-scale feature exploration [15], [16], multi-task joint learning [17], [18], uncertainty-aware learning [14], multi-source information fusion [19], [20], and generative segmentation [21]. The latter generally utilizes scribbles or points as supervision signals, such as contrast and relation model [4] and SAM-guided learning [5], which greatly reduces manual annotation. For more related work, please refer to [22]. Nevertheless, large-scale data annotation is essential.

2.2 Zero-Shot Learning

Lampert *et al.* [23] firstly introduced Zero-shot learning (ZSL), a method that aims to accumulate knowledge from various datasets and identify classes that are not present in the training data. Recently, foundation models such as CLIP [11], [24] and SAM [10] have showcased strong zero-shot capabilities. CLIP leverages a large-scale dataset from web pages, demonstrating impressive zero-shot and open-vocabulary capabilities. Similarly, SAM exhibits strong zero-shot generalization, although it may face challenges with segmenting camouflaged objects [25]. Notably, achieving impressive zero-shot performance often relies on carefully crafted prompts to guide the segmentation process.

Li *et al.* [6] proposes a novel problem called Zero-Shot Camouflaged Object Detection, the first work to detect camouflaged objects of unseen classes in a zero-shot learning setting. Similarly, Pang *et al.* [7] introduces the Open-Vocabulary Camouflaged Object Segmentation (OVCOS) task, which requires the model to perform open-vocabulary segmentation of camouflaged objects and retrieve the most likely object class from a set of unseen object classes. However, both approaches focus on specific classes of objects, aiming to segment unseen categories. This requires the model to be trained on camouflaged objects

from seen classes, meaning that it cannot eliminate the need for COS datasets. Recently, GenSAM [8] and MMCPF [9] have utilized prompt engineering to integrate SAM [10] and M-LLM for zero-shot camouflaged object segmentation. While these methods do not require additional post-training on COS datasets, they still encounter high computational costs during inference.

2.3 Prompt Guidance

Prompt guidance plays a crucial role in multi-modal learning. In SAM [10], prompts such as points, boxes, and rough masks have been effectively utilized to enhance the object segmentation process. In foreground segmentation tasks, modalities like thermal and depth maps are commonly employed, particularly in SOS and COS tasks. Thermal maps provide valuable information about an object’s heat characteristics, and in the SOS task, prior work [26], [27] has explored the integration of RGB and thermal features to boost segmentation accuracy. Depth maps have also been employed as prompts in both SOS and COS tasks. For example, depth maps were leveraged in SOS by [28], [29], [30], while [31] used them for camouflaged object detection. In the OVCOS framework [7], both depth and contour maps serve as effective prompts. However, thermal and depth maps have limitations in certain scenarios, making text prompts a versatile alternative. Text prompts provide broader applicability compared to thermal and depth maps and can be easily generated by multi-modal large language models (M-LLM), offering an efficient way to guide the segmentation process across diverse tasks.

2.4 Parameter-Efficient Fine-Tuning (PEFT)

PEFT reduces computational and storage needs by fine-tuning a small subset of model parameters while keeping the majority fixed. It mainly includes adapter-based

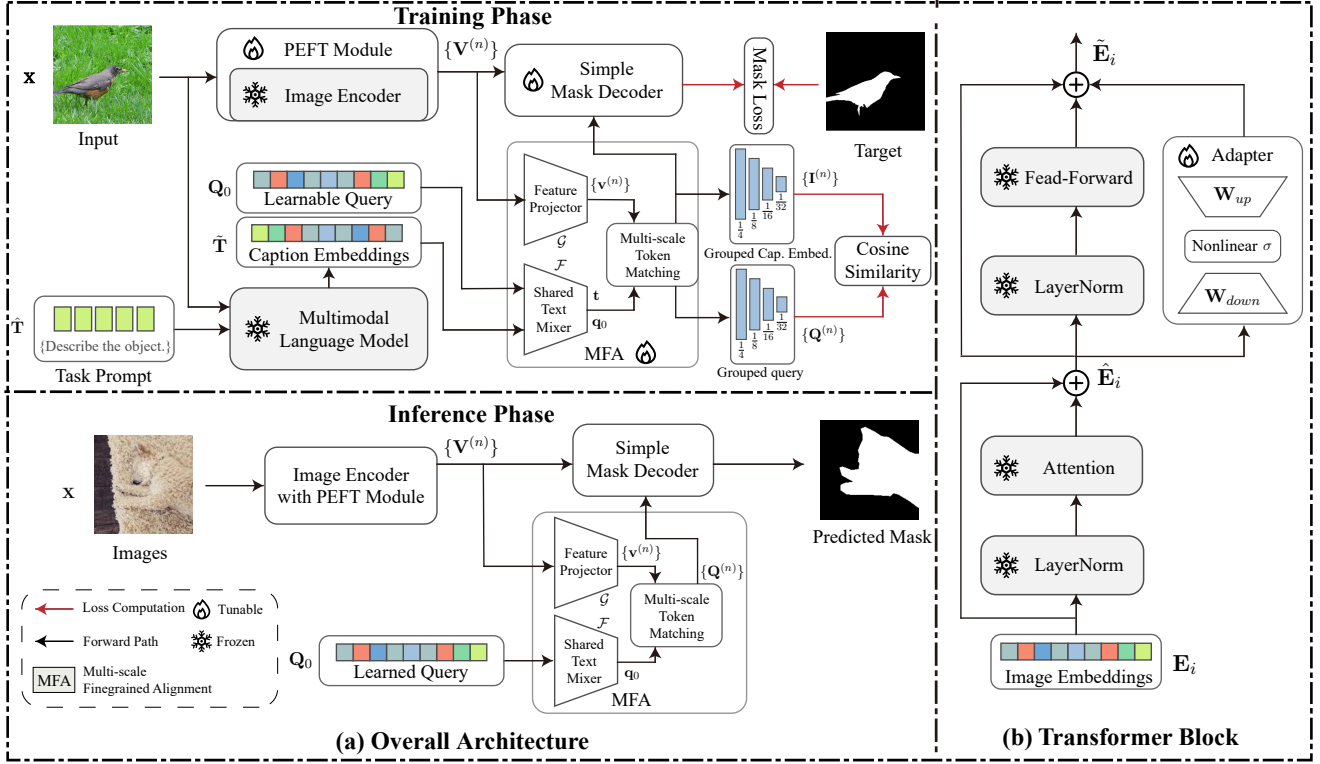


Fig. 3. **Overall Architecture of the Proposed Framework.** In (a), PEFT module is employed during the training phase. Specifically, only PEFT module, the MFA, the query, and the simple mask decoder are fine-tuned, while the remaining parts of the architecture are kept frozen. During inference, the M-LLM is removed and the learned query replaces the caption embeddings. (b) illustrates the implementation of PEFT using Adapter [37] on the transformer block [44] within the image encoder. The bias terms is omitted in the figure.

techniques and Low-Rank Adaptation (LoRA). The adapter approach, one of the techniques used in PEFT, involves inserting small modules called adapters between transformer layers [32]. It can be divided into two categories: In-Block adapter and Branch Adapter. In-block adapter is a type of adapter that is inserted within a transformer block. Two common strategies for in-block adapters are serial and parallel. The serial strategy includes adapters such as NLP Adapter [33], [34] for language tasks and Mona Adapter [35], [36] for vision tasks. On the other hand, AdaptFormer [37] used the parallel strategy. Another type of adapter is the branch adapter, which introduces adapters that branch out from specific transformer layers. Examples of branch adapters include EVP [38], [39] and SAM Adapter [40]. Other PEFT methods include Low-Rank Adaptation (LoRA) [41], Visual Prompt Tuning (VPT) [42], BitFit [43], etc.

3 METHODOLOGY

3.1 Overall Architecture

As discussed earlier, zero-shot scenarios demand effective extraction of low-level semantic information [11], while dense prediction tasks, particularly COS models, rely on high-frequency details to capture object boundaries accurately [12]. To address both these needs, we propose a framework that integrates the strengths of these approaches. Our framework combines the SOS training dataset, known for its ability to learn low-level semantics, with a pre-trained model optimized for dense prediction, thus harnessing both

semantic richness and boundary precision for improved performance.

Specifically, our image encoder, pre-trained using masked image modeling (MIM), is fine-tuned on the SOS dataset, harnessing the strengths of both methods: low-frequency feature learning from the training set and high-frequency feature extraction from MIM. Building on the success reported in [13], we further integrate captions generated by Multimodal Large Language Models (M-LLM) to achieve fine-grained alignment, enhancing the model's ability to capture complex semantic features essential for dense prediction tasks.

The proposed framework is composed of several key components, as illustrated in Fig. 3. The first component is an image encoder, initialized with weights from a MIM pre-training phase. This enables the model to leverage the low-level features learned during pre-training. Next, the Parameter-Efficient Fine-Tuning (PEFT) module ensures that the model can learn semantic-level image features while preserving the valuable information from the MIM-learned features.

To enhance the learning of these semantic features, the framework employs Multi-Scale Fine-Grained Alignment (MFA), which effectively captures cross-modal correlations between image and caption (text) embeddings. These caption embeddings are generated by a M-LLM.

Finally, the framework includes a Mask Decoder, which generates the segmentation output. During inference, the M-LLM is deactivated, and a learned query from the training phase serves as a codebook, replacing the caption em-

beddings. This query, in conjunction with the visual embeddings, ensures the generation of accurate segmentation masks.

3.2 Image Encoder with PEFT

An EVA pre-trained [44], [45] models is utilized in this study to leverage the advantages of both MIM and CL pre-training for PEFT.

Parameter-Efficient Finetuning. During training, given an image $\mathbf{X} \in \mathbb{R}^{H \times W \times 3}$, the patch embedding operation divide it into patches and projects these into image embeddings $\mathbf{E}_1 \in \mathbb{R}^{L \times d_v}$ before passing them into the transformer block of the model.

Originally, the transformer block can be formulated as:

$$\hat{\mathbf{E}}_i = \text{Attention}(\text{LN}(\mathbf{E}_i)) + \mathbf{E}_i, \quad (1)$$

$$\tilde{\mathbf{E}}_i = \text{FFN}(\text{LN}(\hat{\mathbf{E}}_i)) + \hat{\mathbf{E}}_i, \quad (2)$$

where i denotes the i^{th} transformer block, \mathbf{E}_i is the image embedding from the $(i-1)^{\text{th}}$ block, such that $\mathbf{E}_i = \tilde{\mathbf{E}}_{i-1}$.

In this work, We used a parallel adapter in [32], [37] to perform PEFT. Given a matrix $\mathbf{Z} \in \mathbb{R}^{L \times d_v}$, the adapter is a low-rank MLP that can be denoted as

$$\text{Adapter}(\mathbf{Z}) = \sigma(\mathbf{Z}\mathbf{W}_{\text{down}} + \mathbf{b}_1)\mathbf{W}_{\text{up}} + \mathbf{b}_2, \quad (3)$$

where σ represents any non-linear activation function, $\mathbf{W}_{\text{down}} \in \mathbb{R}^{d_v \times d_{lr}}$ and $\mathbf{W}_{\text{up}} \in \mathbb{R}^{d_{lr} \times d_v}$ forms a low rank form with $d_{lr} \ll d_v$. In this work, we use ReLU [46] as activation function. Unlike [32], [37], we have removed the layer normalization and added bias terms for the two linear layers. This modification aims to enable the adapter to learn shape-biased features better at the channel level.

Then the adapter represented in Eq. 3 is injected into the branch of FFN within the transformer blocks. The Eq. 2 can be rewritten as

$$\tilde{\mathbf{E}}_i = a_i \cdot \text{Adapter}(\hat{\mathbf{E}}_i) + \text{FFN}(\text{LN}(\hat{\mathbf{E}}_i)) + \hat{\mathbf{E}}_i, \quad (4)$$

where $a_i \in \mathbb{R}$ is a learnable scale factor.

Multi-scale Transform. Motivated from [47], we utilize simple feature pyramids (SFP) to generate multi-scale features. More specifically, the last feature map of image encoder $\tilde{\mathbf{E}}_N \in \mathbb{R}^{L_v \times d_v}$, where $L_v = \frac{HW}{16^2}$, is fed into SFP to produce multi-scale feature maps $\{\mathbf{V}^{(n)}\}$, where $n \in \mathbf{N}$ and $\mathbf{N} = \{4, 8, 16, 32\}$, at scales $\{\frac{HW}{32^2}, \frac{HW}{16^2}, \frac{HW}{8^2}, \frac{HW}{4^2}\}$.

3.3 Caption Embeddings from M-LLM

In our method, we utilize a M-LLM to generate text embeddings as captions. The M-LLM takes both an image and a task prompt as inputs, and processes them to generate a concise caption embedding that captures the necessary information relevant to the concept.

Given an image \mathbf{X} and a task prompt \mathbf{T} , \mathbf{X} and \mathbf{T} are sent to the M-LLM to generate a caption embedding $\tilde{\mathbf{T}} \in \mathbb{R}^{L_t \times d_t}$.

$$\tilde{\mathbf{T}} = \text{M-LLM}(\mathbf{X}, \mathbf{T}). \quad (5)$$

Different prompts offer varied inputs for the language model, capturing different task-related information. Each prompt may lead to different performance outcomes for the model. In Section 4.4, we include an ablation study on the choice of prompts in both zero-shot and supervised learning.

3.4 Multi-Scale Fine-Grained Alignment

Multi-Scale Fine-Grained Alignment (MFA) is a key component of our framework, designed to align the caption embeddings generated by the M-LLM with the image embeddings from the fine-tuned encoder. This process enhances the PEFT module's ability to learn both shape and semantic features. Additionally, we initialize a learnable query to build a codebook, which significantly improves efficiency during inference. By using the codebook as a substitute for the M-LLM, the model bypasses the computationally expensive process of generating caption embeddings, resulting in faster inference times without sacrificing accuracy. This streamlined approach allows for more efficient deployment, particularly in scenarios where low-latency responses are critical.

As shown in Fig. 3, the MFA module consists of three key components: a feature projector, a multi-scale token matching operation (Fig. 4 (a)), and a text mixer (Fig. 4 (b)). The MFA takes both the caption embeddings, $\tilde{\mathbf{T}}$, and the multi-scale image embeddings, $\{\mathbf{V}^{(n)}\}$, as inputs, producing image-grouped caption embeddings, $\{\mathbf{I}^{(n)}\}$, that are compatible with the mask decoder. Additionally, the learnable query \mathbf{Q}_0 is mapped alongside $\{\mathbf{V}^{(n)}\}$ to generate image-grouped queries, $\{\mathbf{Q}^{(n)}\}$.

Multi-scale Token Matching. To achieve the fine-grained alignment and train a codebook, we propose a simple attention-like mechanism that aligns caption tokens and query tokens with image tokens generated by the text mixer and the feature projector. This mechanism, illustrated in Fig. 4 (a), is inspired by techniques from [13], with several modifications implemented to enhance its effectiveness.

During this process, the multi-scale image embeddings $\{\mathbf{V}^{(n)}\}$ are first passed through a feature projector $\mathcal{G} : \mathbb{R}^{L_v^{(n)} \times d_v} \rightarrow \mathbb{R}^{L_v^{(n)} \times d}$, which generates multi-scale image tokens $\{\mathbf{v}^{(n)}\}$. All image embeddings at each scale utilize the same image projector. Similarly, the caption embedding $\tilde{\mathbf{T}}$ and the query \mathbf{Q}_0 are processed by a shared text mixer $\mathcal{F} : \mathbb{R}^{L_t \times d_t} \rightarrow \mathbb{R}^{L_t/2 \times d}$ to compress the embeddings. Therefore, we have the following notations:

$$\mathbf{v}^{(n)} = \mathcal{G}(\mathbf{V}^{(n)}), \quad (6)$$

$$\mathbf{t} = \mathcal{F}(\tilde{\mathbf{T}}), \quad (7)$$

$$\mathbf{q}_0 = \mathcal{F}(\mathbf{Q}_0). \quad (8)$$

For simplicity, we denote the sequence tokens from the mixer is \mathbf{u} , where $\mathbf{u} \in \mathbb{R}^{L_t/2 \times d}$ and $\mathbf{u} \in \{\mathbf{t}, \mathbf{q}_0\}$. Therefore, the entire token matching process can be represented as:

$$\mathbf{A}^{(n)} = \text{TM}(\mathbf{v}^{(n)}, \mathbf{u}). \quad (9)$$

Specifically, The first step is to calculate the similarity and attain the alignment weights from the similarity using min-max normalization along the row.

$$\mathbf{s}^{(n)} = \text{Normalize}_{L_t}(\mathbf{v}^{(n)} \mathbf{u}^\top). \quad (10)$$

The resulting $\mathbf{s}^{(n)}$ is a normalized similarity matrix with a shape of $L_v \times \frac{L_t}{2}$. Then, the alignment weights are sparsified

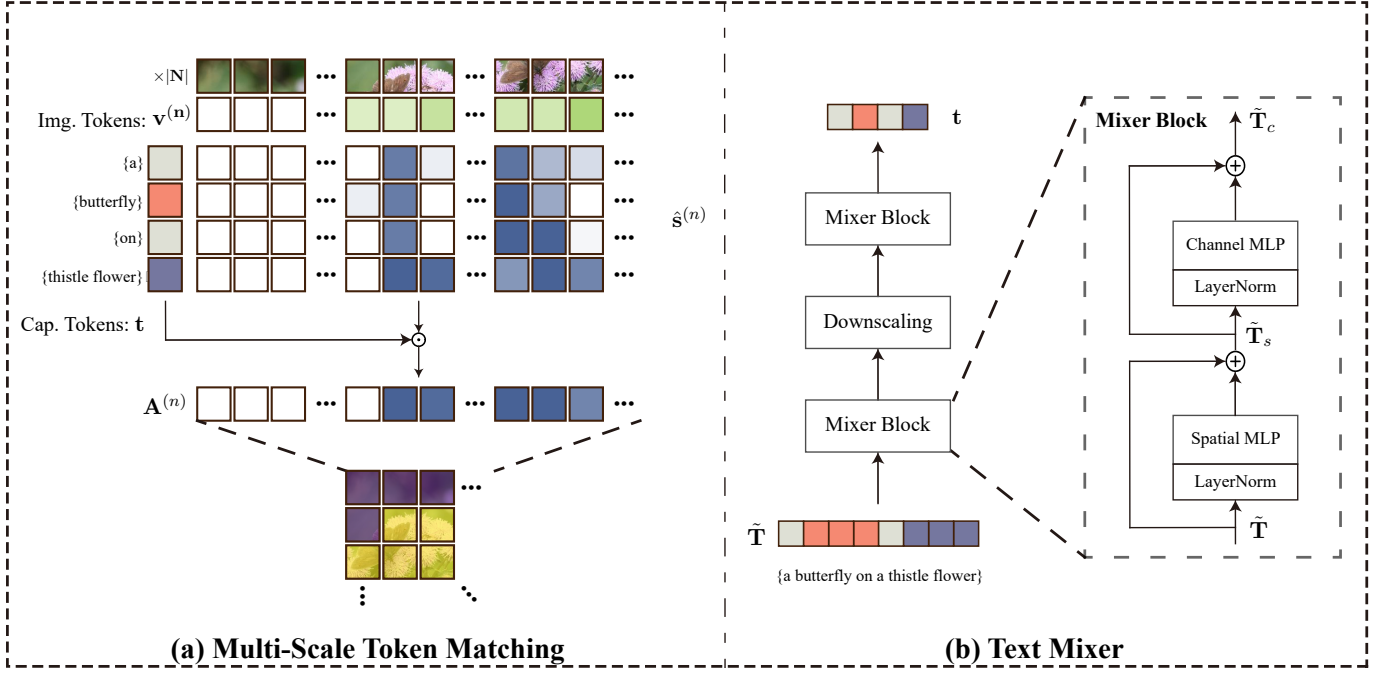


Fig. 4. **Multi-scale Token Match Operation and the structure of Text Mixer.** The left figure highlights how the multi-scale vision tokens and caption tokens are aligned using TM. The right figure provides a closer look at the text mixer, which is composed of two mixer blocks and a down-scaling module.

using a simple threshold strategy. We denote $\mathbf{s}^{(n)} = [s_{ij}^{(n)}]$ and $\hat{\mathbf{s}}^{(n)} = [\hat{s}_{ij}^{(n)}]$, where $1 \leq i \leq L_v^{(n)}$ and $1 \leq j \leq \frac{L_t}{2}$.

$$\hat{s}_{ij}^{(n)} = \begin{cases} s_{ij}^{(n)}, & s_{ij}^{(n)} \geq \frac{1}{L_v^{(n)}} \\ 0, & \text{otherwise.} \end{cases} \quad (11)$$

Every element in $\mathbf{s}^{(n)}$ undergoes a thresholding process. This thresholding is based on the threshold value $1/L_v^{(n)}$. If an element is equal to or greater than the threshold value, its value remains; otherwise, it is assigned a value of 0. Then, we get the image-grouped tokens by

$$\mathbf{A}^{(n)} = \text{Softmax}_{L_t}(\hat{\mathbf{s}}^{(n)}) \mathbf{u}, \quad (12)$$

where $\text{Softmax}_{L_t}(\cdot)$ denotes the softmax operation along the row.

This operation is applied to caption tokens and query tokens from the mixer separately. Subsequently, by replacing \mathbf{u} with caption and query tokens \mathbf{t} and \mathbf{q}_0 respectively, the multi-scale TM operation produces the multi-scale image-grouped caption embeddings $\{\mathbf{I}^{(n)}\}$ and the image-grouped queries $\{\mathbf{Q}^{(n)}\}$. This process can be expressed using Eq. 9 as follows:

$$\mathbf{I}^{(n)} = \text{TM}(\mathcal{G}(\mathbf{V}^{(n)}), \mathcal{F}(\tilde{\mathbf{T}})), \quad (13)$$

$$\mathbf{Q}^{(n)} = \text{TM}(\mathcal{G}(\mathbf{V}^{(n)}), \mathcal{F}(\mathbf{Q}_0)). \quad (14)$$

For caption tokens, this operation produces image-grouped caption embeddings that are aligned with the image embeddings. For example, if the caption mentions a “poodle”, the corresponding patches in the image-grouped caption embeddings representing the “poodle” will be activated, while the remaining patches will be deactivated. Furthermore, by employing multi-scale TM, we obtain the image-grouped query $\{\mathbf{Q}^{(n)}\}$ for the codebook learning.

Text Mixer and Feature Projector. Text mixer and image projector are designed to learn non-linear transformations. Thus, we can learn a more expressive and flexible mapping between the visual representations and the aligned feature space, beyond what a simple linear projection could achieve. The text mixer \mathcal{F} applies both spatial and channel transformations to the caption sequence, allowing for more fine-grained processing of the textual representations. MLP based mixer, are generally more computationally efficient than attention-based architecture. This text mixer is composed of two mixer block and a linear down-scaling in the middle. Each block contains a spatial mixer and a channel mixer based on MLP. The mixer block can be formulated as follows:

$$\tilde{\mathbf{T}}_s = \text{MLP}(\text{LN}(\tilde{\mathbf{T}})^T) + \tilde{\mathbf{T}}, \quad (15)$$

$$\tilde{\mathbf{T}}_c = \text{MLP}(\text{LN}(\tilde{\mathbf{T}}_s)) + \tilde{\mathbf{T}}_s. \quad (16)$$

Then, $\tilde{\mathbf{T}}_c$ is down-scaled by a learnable matrix $\mathbf{W}_{/2} \in \mathbb{R}^{\frac{L_t}{2} \times d}$ and another mixer block is apply on it to get the final \mathbf{t} .

For image embeddings, the feature projector is a simple channel MLP which maps $\mathbb{R}^{L_v^{(n)} \times d_v}$ to $\mathbb{R}^{L_v^{(n)} \times d}$ allowing us to adjust the channel dimensionality of the image embeddings to match the channel dimensionality of the caption embeddings.

3.5 Mask Decoder

We utilize an all-MLP decoder to maintain a straightforward design. As illustrated in Fig. 5, the mask decoder comprises nine MLP layers in total. It takes both multi-scale image embeddings $\{\mathbf{V}^{(n)}\}$ and grouped tokens $\{\mathbf{A}^{(n)}\}$ as inputs.

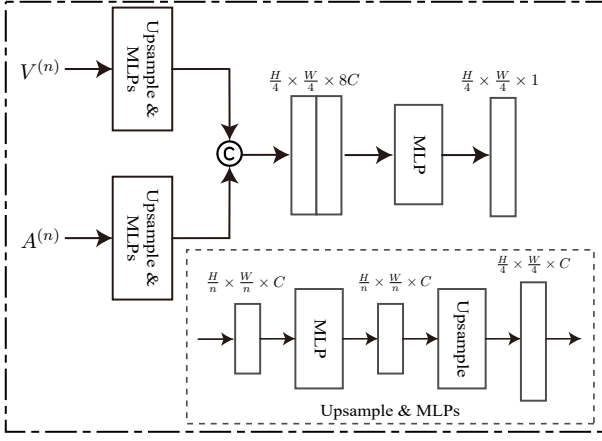


Fig. 5. The structure of simple mask decoder. We use several MLPs and upsampling modules to maintain a simple design.

These two representations are then fused using a simple concatenation operation. The fused representation is processed through an MLP to produce the final output mask logits.

3.6 Inference with Learned Query

During the inference phase, the M-LLM is not used. Instead, we replace the caption embeddings with the learned query \mathbf{Q}_0 . In the training phase, $\mathbf{I}^{(n)}$ serves as $\mathbf{A}^{(n)}$ for the input to the simple mask decoder. During inference, since the M-LLM is replaced, $\mathbf{Q}^{(n)}$ is used as $\mathbf{A}^{(n)}$ for the input to mask decoder. Surprisingly, in Section 4.4, we demonstrate that this approach outperforms using caption embedding from the M-LLM during inference.

3.7 Loss Function

The total loss can be represented as a weighted sum of mask loss \mathcal{L}_{mask} and query loss \mathcal{L}_q . The mask loss is used to regularize the segmentation mask generation. The query loss is used to regularize the query to learn a codebook.

$$\mathcal{L} = \mathcal{L}_{mask} + \lambda \mathcal{L}_q, \quad (17)$$

with $\lambda > 0$.

Mask Loss. We use BCE, DICE, and UAL [20] for mask loss. The BCE loss function is a fundamental object function in various binary image segmentation tasks. The DICE loss and UAL loss are used to increase the confidence.

$$\mathcal{L}_{mask} = \lambda_{bce} \mathcal{L}_{bce} + \lambda_{dice} \mathcal{L}_{dice} + \lambda_{ual} \mathcal{L}_{ual}. \quad (18)$$

Query Loss. Cosine similarity is utilized to learn the query effectively. For each scale of the grouped caption embeddings and their corresponding queries, we compute the cosine similarity to evaluate their relationship.

$$\mathcal{L}_q = 1 - \frac{1}{|\mathbf{N}|} \sum_{n \in \mathbf{N}} \frac{\mathbf{I}^{(n)} \cdot \mathbf{Q}^{(n)}}{\|\mathbf{I}^{(n)}\|_2 \cdot \|\mathbf{Q}^{(n)}\|_2}. \quad (19)$$

4 EXPERIMENTS

4.1 Experiment Setting

Zero-shot Setting. To perform zero-shot camouflaged object segmentation (COS), we used the salient object segmentation dataset DUTS [48] during the training phase. During the evaluation phase, we employed four widely used COS datasets to thoroughly assess the model’s zero-shot capabilities: the test sets of CAMO [49], COD10K [2], CHAMELEON [50], and NC4K [3]. In the zero-shot learning setting for COS, models were trained for 20 epochs with a linear warm-up over the first 6 epochs on DUTS, using a batch size of 10.

Supervised Learning Setting. In supervised camouflaged object segmentation (COS), we used a combined training set from CAMO and COD10K, while the remaining COS datasets served as the test datasets. Specifically, CAMO [49] provided 1,000 training images and 250 testing images featuring diverse camouflaged objects. COD10K [2] included 3,040 training samples and 2,026 test samples. CHAMELEON [50] and NC4K [3] contained 76 test samples and 4,121 samples, respectively. For supervised learning in COS, we trained the models for 50 epochs with a linear warm-up of 10 epochs.

Implementation Details. Our method was implemented using the PyTorch framework and the experiments were conducted on a GeForce RTX4060Ti GPU. In our implementation, we utilized BLIP2 [51] offline to save GPU memory, specifically employing the *blip2-opt* model as the M-LLM component. The standalone image encoder was a pre-trained EVA02-L [44] model, while the remaining modules were randomly initialized. To optimize the attention mechanism and further reduce GPU memory usage, we utilized the FlashAttention operator [52]. We employed the AdamW [53] optimizer for all experiments, with an initial learning rate of 1.5×10^{-4} and a cosine decay scheduler. During the training phase, we performed data augmentation by resizing input images to 384×384 pixels and applying random horizontal flips.

Loss Weights. The loss function employed for training was a combination of mask loss and query loss see in Section 3.7. We employed a straightforward approach for combining loss weights. In zero-shot, for the mask loss \mathcal{L}_{mask} , we set $\lambda_{bce} = 1$, and $\lambda_{dice} = 0.5$. The UAL loss was not included in this setting. The weight for the query loss was set to $\lambda = 0.5$. In supervised training, we maintained the same values for λ_{bce} , λ_{dice} , and λ . To enhance the confidence of the segmentation map, we included an additional UAL loss [20]. Instead of using a dynamic loss weight for the UAL loss as described in [20], we fixed the weight at $\lambda_{ual} = 1$.

Evaluation Metrics. To thoroughly evaluate the model’s performance, we employed four widely-used metrics: weighted F-measure (F_β^w) [54], mean absolute error (MAE), S-measure (S_α) [55], and mean E-measure (E_ϕ) [56], [57].

4.2 Zero-Shot Results

Comparison Settings. We retrained the comparison methods, including VST [58], SINet-V2 [2], CRNet [4], EVP-Segformer [38], [59], and EVP-EVA02-L [38], [44] using the DUTS dataset and their original training settings to ensure a fair comparison.

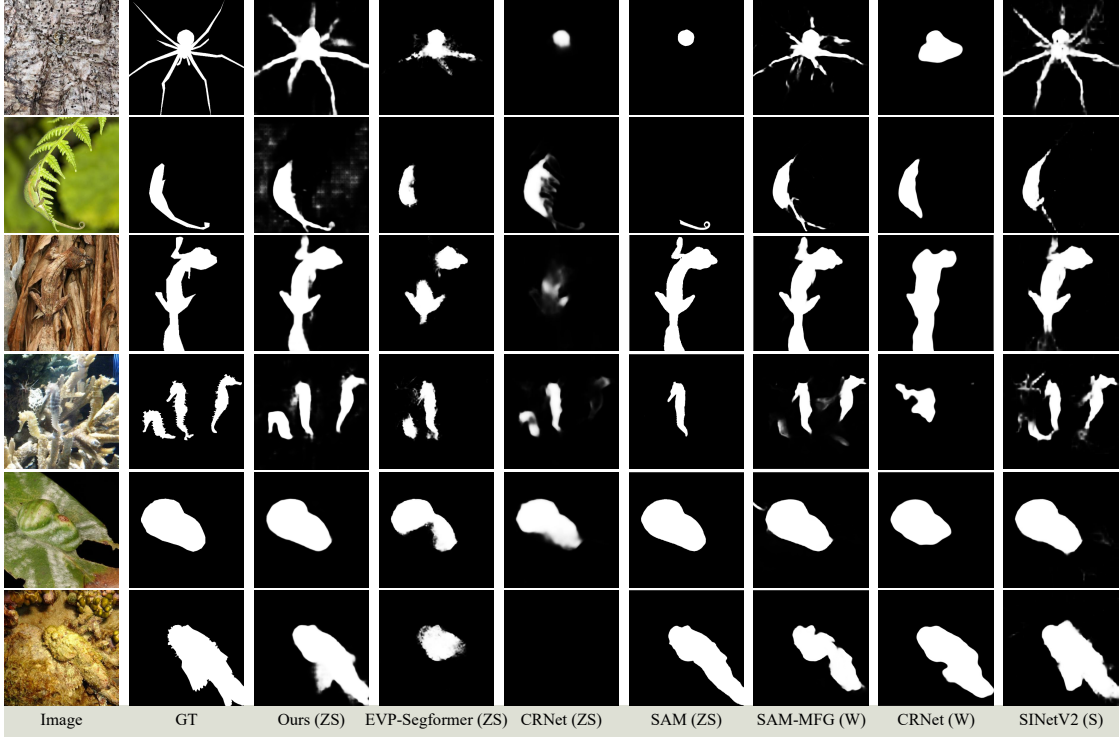


Fig. 6. Comparison with Other Methods under Zero-shot, Weakly Supervised, and supervised Learning Setting. We compare our proposed method with existing approaches under zero-shot (ZS), weakly supervised (W), and supervised (S) learning settings. The results are presented for the COD10K [2], and CAMO [49] datasets.

Discussion. In Tab.1, we presented the comparison results of our method with other methods specialized on four different datasets. The methods include several supervised approaches like VST [58], SiNetV2 [2], EVP [38], [39] using zero-shot training strategy, and weakly supervised methods like CRNet [4] and SAM-MFG [5].

Our method demonstrates strong performance in zero-shot COS task, showing the highest weighted F-measure compared to other methods under zero-shot setting in four datasets. Notably, a comprehensive analysis of Tab.1 reveals an implicit trend: while certain methods excel on individual datasets (*e.g.* CRNet [4] achieving a weighted F-measure of 0.744 on the CHAMELEON [50] dataset), their performance diminishes on other datasets (*e.g.* CRNet [4] achieving a weighted F-measure of only 0.576 on the COD10K [2] dataset). In contrast, our method consistently maintains strong performance across all four datasets, with weighted F-measures exceeding 0.710, MAE values below 0.107, S-measure values surpassing 0.775, and mean E-measure values exceeding 0.800.

In Fig.6, we present visual comparisons between our method and other COS approaches under zero-shot setting. The results demonstrate that our proposed method outperforms the alternative methods in terms of mask prediction for the majority of samples.

4.3 Supervised Learning Results

In the context of supervised learning, we evaluated our framework against 14 other methods across four different datasets. As shown in Tab. 1, our framework consistently outperforms the alternatives, with particularly strong re-

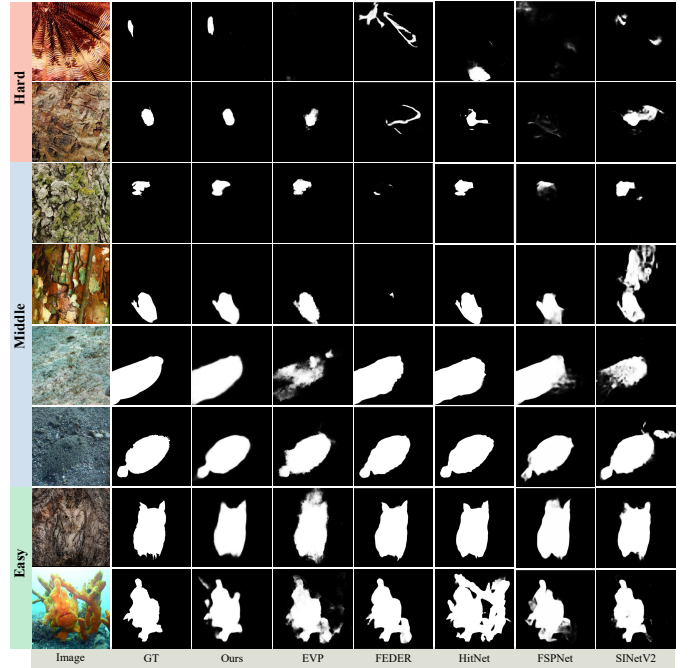


Fig. 7. Visualization of the predicted masks of our methods and others in the supervised learning setting. The figure presents results for hard, medium, and easy examples. Each row shows the original image, ground truth (GT), and outputs from various methods: Ours, EVP, FEDER, HitNet, FSPNet, and SiNetV2.

sults on the CAMO and NC4K datasets, where it achieves the highest weighted F-measure scores. This demonstrates our model's superior ability to confidently detect camou-

TABLE 1

Quantitative results of zero-shot (ZS) and supervised camouflaged object segmentation methods. Several weakly-supervised methods (WS) are also included for comparison in the zero-shot setting. It is important to note that the ZS settings in some existing methods differ from ours, as illustrated in Fig. 2. The best three results are highlighted in red, blue, and green, respectively.

Zero-Shot (ZS) and Weakly-Supervised (WS) Setting																			
Methods	Pub.	Sup.	Data	CAMO				NC4K				COD10K				CHAMELEON			
				$F_{\beta}^w \uparrow$	MAE \downarrow	$S_{\alpha} \uparrow$	$E_{\phi} \uparrow$	$F_{\beta}^w \uparrow$	MAE \downarrow	$S_{\alpha} \uparrow$	$E_{\phi} \uparrow$	$F_{\beta}^w \uparrow$	MAE \downarrow	$S_{\alpha} \uparrow$	$E_{\phi} \uparrow$	$F_{\beta}^w \uparrow$	MAE \downarrow	$S_{\alpha} \uparrow$	$E_{\phi} \uparrow$
SCWSSOD [60]	AAAI21	WS	COD10K	.618	.102	.713	.815	-	-	-	-	.546	.049	.710	.805	.714	.053	.792	.881
TEL [61]	CVPR22	WS	COD10K	.635	.133	.645	.674	.711	.085	.766	.795	.604	.063	.727	.803	.645	.094	.746	.751
CRNet [4]	AAAI23	WS	COD10K	.641	.092	.735	.815	.741	.080	.758	.796	.576	.049	.733	.805	.744	.046	.818	.897
SAM-MFG [5]	NeurIPS23	WS	COD10K	.679	.102	.718	.757	.799	.057	.813	.859	.698	.039	.790	.856	.728	.056	.805	.868
SAM [10]	ICCV23	ZS	SA-1B	.597	.160	.643	.639	.696	.078	.767	.776	.673	.093	.730	.737	.595	.207	.635	.647
SAM2 [62], [63]	arXiv24	ZS	SA-V	.184	.236	.444	.401	.251	.186	.512	.482	.271	.134	.549	.521	-	-	-	-
GenSAM [8]	AAAI24	ZS	SA-1B	.659	.113	.719	.775	.665	.087	.754	.781	.681	.067	.775	.838	.680	.090	.764	.807
MMCPF [9]	MM24	ZS	SA-1B	.683	.101	.751	.772	.686	.079	.769	.796	.596	.062	.769	.826	-	-	-	-
VST [58]	ICCV21	ZS	DUTS	.563	.154	.651	.683	.685	.091	.752	.790	.544	.087	.676	.732	.548	.113	.659	.686
SINet-V2 [2]	TPAMI22	ZS	DUTS	.437	.188	.583	.575	.551	.127	.667	.668	.404	.103	.604	.598	.291	.165	.515	.461
CRNet [4]	AAAI23	ZS	DUTS	.445	.156	.593	.575	.599	.096	.694	.697	.443	.079	.611	.590	.377	.129	.562	.509
EVP-Segformer [38]	CVPR23	ZS	DUTS	.637	.137	.701	.733	.756	.071	.788	.822	.652	.062	.716	.764	.642	.091	.713	.713
EVP-EVA02-L [38], [44]	-	ZS	DUTS	.671	.125	.750	.775	.783	.069	.837	.862	.674	.068	.781	.816	.663	.089	.760	.768
Ours	-	ZS	DUTS	.729	.105	.788	.814	.818	.054	.861	.882	.717	.055	.808	.832	.720	.067	.805	.817

Supervised Setting																		
Methods	Pub.	Input Size	CAMO				NC4K				COD10K				CHAMELEON			
			$F_{\beta}^w \uparrow$	MAE \downarrow	$S_{\alpha} \uparrow$	$E_{\phi} \uparrow$	$F_{\beta}^w \uparrow$	MAE \downarrow	$S_{\alpha} \uparrow$	$E_{\phi} \uparrow$	$F_{\beta}^w \uparrow$	MAE \downarrow	$S_{\alpha} \uparrow$	$E_{\phi} \uparrow$	$F_{\beta}^w \uparrow$	MAE \downarrow	$S_{\alpha} \uparrow$	$E_{\phi} \uparrow$
SINet [1]	CVPR20	352	.606	.100	.751	.829	.723	.058	.808	.871	.551	.051	.771	.806	.740	.444	.869	.891
LSR [3]	CVPR21	352	.696	.105	.787	.854	.766	.048	.840	.907	.673	.037	.804	.892	.673	.037	.804	.892
ZoomNet [14]	CVPR22	384	.752	.066	.820	.892	.784	.043	.853	.912	.729	.029	.838	.911	.845	.023	.902	.958
SegMaR [16]	CVPR22	352	.724	.072	.805	.864	.781	.046	.841	.907	.686	.036	.813	.890	.828	.032	.888	.935
SINet-V2 [2]	TPAMI22	352	.743	.070	.820	.895	.790	.060	.822	.885	.680	.037	.815	.906	.816	.030	.888	.942
OSFormer [64]	ECCV22	384	.767	.073	.799	.858	.790	.049	.832	.891	.701	.034	.811	.811	.836	.028	.891	.939
HitNet [65]	AAAI23	704	.806	.056	.844	.904	-	-	-	-	.804	.023	.869	.936	-	-	-	-
PENet [66]	IJCAI23	352	.771	.063	.828	.890	.795	.042	.855	.912	.723	.031	.831	.908	.851	.024	.902	.960
DaCOD [67]	MM23	448	.796	.051	.855	.902	.814	.036	.874	.912	.729	.028	.840	.906	-	-	-	-
FEDer [18]	CVPR23	384	.807	.066	.836	.897	.824	.042	.862	.913	.748	.029	.844	.911	.856	.026	.903	.947
FSPNet [15]	CVPR23	384	.799	.050	.856	.899	.816	.035	.879	.915	.735	.026	.851	.895	-	-	-	-
EVP-Segformer [38]	CVPR23	352	.777	.059	.846	.895	.818	.047	.855	.901	.742	.029	.843	.907	.795	.036	.871	.917
ZoomNeXt [20]	TPAMI24	384	.857	.041	.889	.945	.863	.028	.903	.951	.827	.018	.898	.956	.885	.018	.924	.975
EVP-EVA02-L [38], [44]	-	352	.838	.050	.895	.924	.854	.037	.902	.933	.784	.030	.878	.924	.836	.035	.901	.937
Ours	-	384	.887	.041	.901	.933	.897	.033	.905	.933	.845	.025	.890	.923	.895	.028	.917	.944

flagged objects in these challenging datasets.

On the COD10K and CHAMELEON dataset, our framework achieves the highest weighted F-measure scores of 0.845 and 0.895 respectively; however, it slightly trails other methods, such as ZoomNext and HitNet, particularly in S-measure and E-measure. This performance discrepancy may be attributed to ZoomNext utilizing three different resolutions derived from the original 384-resolution image as raw inputs, and HitNet employs a high resolution of 704 to enhance segmentation detail. Overall, these experimental results clearly demonstrate that our approach surpasses many other supervised learning models in tackling the COS task, delivering competitive performance on multiple datasets.

In Fig. 7, we present visual comparisons between our method and other COS approaches under supervised learning setting. The results indicate that our proposed method outperforms the alternative approaches across various levels of difficulty in mask prediction for the majority of

samples.

4.4 Ablation Study

Our method employs a straightforward alignment strategy through the use of MFA. In order to assess the effectiveness of each component within MFA, we conducted ablation studies on COS datasets.

The Caption Strategy. In Tab. 2, we compare two captioning strategies for the inference phase: captions generated from the M-LLM and those derived from the codebook, utilizing the weighted F-measure metric. Our findings indicate that the codebook consistently outperforms captions from the M-LLM across all datasets and application scenarios, demonstrating its overall superior performance.

The MFA components. In Tab. 2, we evaluated four different approaches for processing and analyzing image features: using a Linear Projector alone, utilizing an MLP Projector alone, and incorporating multi-scale information for image processing with both methods separately. The com-

TABLE 2
Ablation study on various aspects. The rows highlighted in gray represent our method (default setting).

Method		Supervised				Zero-Shot			
		COD10K	CAMO	NC4K	CHAMELEON	COD10K	CAMO	NC4K	CHAMELEON
Caption Strategy	M-LLM Caption	.826	.872	.886	.877	.708	.720	.809	.712
	Codebook	.845	.887	.897	.895	.717	.729	.818	.720
MFA Component	Linear w/o multi-scale	.819	.867	.879	.877	.669	.664	.781	.670
	MLP Proj. & Mixer w/o multi-scale	.816	.878	.873	.871	.698	.730	.797	.704
	Linear + multi-scale	.845	.878	.896	.895	.696	.673	.800	.673
	MLP Proj. & Mixer + multi-scale	.845	.887	.897	.895	.717	.729	.818	.720
Channels	64 Channels (72.0K MFA Params)	.799	.841	.842	.837	.691	.678	.800	.692
	128 Channels (0.204M MFA Params)	.819	.853	.860	.859	.714	.710	.818	.705
	256 Channels (0.664M MFA Params)	.845	.887	.897	.895	.717	.729	.818	.720
	512 Channels (2.37M MFA Params)	.841	.882	.889	.893	.498	.517	.621	.536
PEFT Module	LoRA	.824	.881	.878	.878	.692	.677	.798	.633
	Adapter	.845	.887	.897	.895	.717	.729	.818	.720

bined approach of Multi-scale and MLP Projector demonstrates superior performance. This suggests that integrating multi-resolution inputs effectively improves model accuracy. Thus, we selected the MLP Proj. & Mixer + multi-scale approach.

The Channels of MFA Projector and Mixer. Furthermore, Tab. 2 compared the performance of four different channel parameters corresponding to feature projector and text mixer. After considering the trade-off between performance and the number of parameters, we set channels to 256 to achieve an optimal balance.

The PEFT module. We evaluated two different Parameter-Efficient Fine-Tuning (PEFT) modules: LoRA [41] and Adapter [37]. The results were tested across four COS datasets. In Tab. 2, we present the performance of models using LoRA and Adapter in both supervised learning and zero-shot settings. Generally, Adapter outperforms LoRA. This may be due to the tuning of LoRA potentially obscuring local patterns learned during the MIM pre-training, as these local features might be influenced by shape and semantic features from salient objects. In contrast, Adapter does not face this issue, as the FFN in the transformer block acts as a key-value memories for attention [68]. By using Adapter, we can effectively learn shape and semantic features without compromising the local patterns established during the MIM phase, enabling better extraction of useful features for zero-shot COS.

The task prompts. In Tab. 3, we present the impact of various prompts on model performance. In the zero-shot setting, we used the SOS task prompt and observed that the instruction "Describe the image." yielded the best results. This can be attributed to the fact that describing the entire image allows the codebook to capture a more comprehensive and global representation. Conversely, limiting the description to only salient objects may constrain the semantic space, reducing the model's ability to generalize. In the supervised learning setting, we employed the COS task prompt, where "Describe the camouflaged animal." led to the highest performance.

Interestingly, replacing "camouflaged animal" with "camouflaged object" introduced ambiguity between salient and camouflaged objects in the M-LLM's output, which negatively affected the model's accuracy. By specifying camouflaged objects and providing detailed descriptions, we enable the codebook to learn more effective representations

TABLE 3
Ablation study examining the influence of different prompts during training on the weighted F-measure (F_β^w) for CAMO and COD10K datasets. In zero-shot setting, we use SOS task prompt. In supervised learning setting, we use COS task prompt. The results demonstrate how prompt selection affects model performance.

ID	Prompt	CAMO	COD10K
SOS			
1	"The object."	.697	.693
2	"The salient object."	.693	.694
3	"Which object is salient?"	.697	.692
4	"Describe the image."	.729	.717
5	"Describe the object."	.716	.710
6	"Describe the salient object."	.717	.710
COS			
7	"The camouflaged object."	.866	.823
8	"The camouflaged animal"	.879	.838
9	"Which animal is camouflaged?"	.879	.840
10	"Describe the image."	.886	.842
11	"Describe the camouflaged animal."	.887	.845

tailored to these specific objects, resulting in improved model performance.

4.5 Analysis of Running Times (FPS)

Using the learned query during inference simplifies our pipeline, enabling it to achieve frame rates comparable to current state-of-the-art models. We evaluated our method on 100 images using a NVIDIA RTX 4060Ti GPU paired with an i7-13790F CPU. The results are presented in Fig. 8. The size of the markers in the plot reflects the number of parameters in each model, with larger markers representing models with more parameters. The plot highlights the trade-offs between model size, speed, and performance. For the performance, we report the F_β^w score for each method on the CAMO dataset.

EVP-EVA02-L achieves the highest FPS at 24.2, with an F_β^w score of 0.838 and 304 million parameters. **EVP-Segformer** and **FSPNet** offer moderate FPS (19.2 and 13.4) and F_β^w scores (0.777 and 0.799), with parameter counts of 67.7M and 274M, respectively. **ZoomNext** provides a balance with 7.5 FPS and a high F_β^w score of 0.857, using 84.8 million parameters. **SAM**, with the largest parameter count (636M), operates at only 0.3 FPS, achieving an F_β^w score of 0.597. Finally, **Our method** delivers an impressive F_β^w score

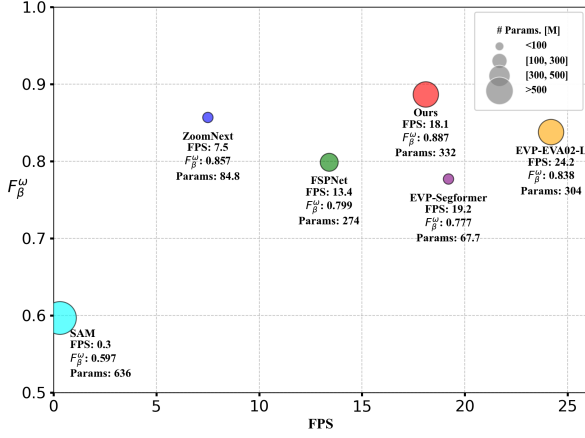


Fig. 8. Comparison of models based on F_{β}^w score, FPS, and number of parameters. Larger markers indicate models with more parameters.

TABLE 4
Additional experiment on polyp segmentation.

Methods	Kvasir				ETIS			
	$F_{\beta}^w \uparrow$	MAE \downarrow	$S_{\alpha} \uparrow$	$E_{\phi} \uparrow$	$F_{\beta}^w \uparrow$	MAE \downarrow	$S_{\alpha} \uparrow$	$E_{\phi} \uparrow$
Zero-shot								
CLIP Surgery+SAM [10], [69]	-	-	-	-	.047	.537	.272	.296
GenSAM [8]	-	-	-	-	.090	.205	.430	.554
Ours	.426	.094	.633	.575	.330	.087	.620	.570
Supervised								
UNet [70]	.794	.055	.858	.893	.366	.036	.843	.876
PraNet [71]	.885	.030	.915	.948	.600	.031	.794	.841
Ours	.977	.008	.973	.982	.760	.018	.882	.899

of 0.887 at 18.1 FPS, with 332M parameters. As illustrated, our approach strikes the best balance between performance, FPS, and parameter efficiency, offering competitive speed and accuracy with an affordable parameter size.

5 ADDITIONAL EXPERIMENTS ON POLYP SEGMENTATION

To showcase the practical applications of our framework, we performed additional experiments in the medical domain, focusing on polyp segmentation. In the zero-shot setting, we aimed to transfer knowledge from camouflaged object segmentation to polyp segmentation, utilizing our pre-trained COS model for direct inference on polyp segmentation tasks. For the supervised learning scenario, we trained the model using the Kvasir dataset [72] and evaluated its performance on the Kvasir and ETIS test sets [73], which are widely used for benchmarking. The Kvasir dataset typically serves as the training set, while the ETIS test set is part of the standard evaluation suite. The results, as presented in Table 4, demonstrate that our model achieves state-of-the-art performance in zero-shot polyp segmentation by effectively transferring knowledge from camouflaged object segmentation. Furthermore, our method achieved the highest weighted F-measure scores of 97.7% on the Kvasir test set and 76.0% on the ETIS test set.

6 CONCLUSION

In this paper, we tackled the challenging problem of zero-shot Camouflaged Object Segmentation (ZSCOS) without

the need for camouflaged object annotations. We proposed a novel framework that integrates the strengths of both vision and language models, leveraging a pre-trained Masked Image Modeling (MIM) encoder and Multimodal Large Language Models (M-LLM) to effectively align visual and semantic features. By incorporating Salient Object Segmentation (SOS) datasets and fine-grained alignment strategies, our approach bridges the gap between COS and SOS, enabling effective zero-shot transfer. Our key contributions also include the introduction of a codebook that substitutes the need for M-LLM during inference, significantly reducing computational overhead while maintaining high performance. Through extensive experiments, our method demonstrated state-of-the-art results in zero-shot COS, achieving impressive F_{β}^w scores on the CAMO and COD10K datasets, and competitive results in polyp segmentation. Furthermore, we showed that our approach performs competitively in both zero-shot and supervised settings, highlighting its broad applicability across various segmentation tasks.

Beyond numerical advancements, our work paves the way for new possibilities in zero-shot learning for complex segmentation tasks, providing an efficient, scalable, and high-performance solution adaptable to diverse applications. The flexibility of our framework enables it to be applied across a broad spectrum of domains, from medical imaging to environmental monitoring, where annotated data is scarce or unavailable. Future research could focus on extending this approach to other challenging dense prediction tasks, utilizing larger datasets to provide richer semantic information, refining the codebook mechanism, and further optimizing the trade-off between computational efficiency and segmentation accuracy.

REFERENCES

- [1] D.-P. Fan, G.-P. Ji, G. Sun, M.-M. Cheng, J. Shen, and L. Shao, "Camouflaged object detection," in *CVPR*, 2020.
- [2] D.-P. Fan, G.-P. Ji, M.-M. Cheng, and L. Shao, "Concealed object detection," *IEEE TPAMI*, vol. 44, no. 10, pp. 6024–6042, 2022.
- [3] Y. Lyu, J. Zhang, Y. Dai, A. Li, B. Liu, N. Barnes, and D.-P. Fan, "Simultaneously localize, segment and rank the camouflaged objects," in *CVPR*, 2021.
- [4] R. He, Q. Dong, J. Lin, and R. W.H. Lau, "Weakly-supervised camouflaged object detection with scribble annotations," *AAAI*, vol. 37, no. 1, pp. 781–789, Jun. 2023.
- [5] C. He, K. Li, Y. Zhang, G. Xu, L. Tang, Y. Zhang, Z. Guo, and X. Li, "Weakly-supervised concealed object segmentation with sam-based pseudo labeling and multi-scale feature grouping," *NeurIPS*, vol. 36, 2024.
- [6] H. Li, C.-M. Feng, Y. Xu, T. Zhou, L. Yao, and X. Chang, "Zero-shot camouflaged object detection," *IEEE TIP*, vol. 32, pp. 5126–5137, 2023.
- [7] Y. Pang, X. Zhao, J. Zuo, L. Zhang, and H. Lu, "Open-vocabulary camouflaged object segmentation," in *ECCV*, 2024.
- [8] J. Hu, J. Lin, S. Gong, and W. Cai, "Relax image-specific prompt requirement in sam: A single generic prompt for segmenting camouflaged objects," in *Proceedings of the AAAI Conference on Artificial Intelligence*, vol. 38, no. 11, 2024, pp. 12511–12518.
- [9] L. Tang, P.-T. Jiang, Z. Shen, H. Zhang, J. Chen, and B. Li, "Chain of visual perception: Harnessing multimodal large language models for zero-shot camouflaged object detection," in *ACM Multimedia 2024*, 2024.
- [10] A. Kirillov, E. Mintun, N. Ravi, H. Mao, C. Rolland, L. Gustafson, T. Xiao, S. Whitehead, A. C. Berg, W.-Y. Lo, P. Dollár, and R. Girshick, "Segment anything," in *ICCV*, 2023.
- [11] A. Radford, J. W. Kim, C. Hallacy, A. Ramesh, G. Goh, S. Agarwal, G. Sastry, A. Askell, P. Mishkin, J. Clark, G. Krueger, and I. Sutskever, "Learning transferable visual models from natural language supervision," in *ICML*, vol. 139, 2021, pp. 8748–8763.

- [12] N. Park, W. Kim, B. Heo, T. Kim, and S. Yun, "What do self-supervised vision transformers learn?" in *ICLR*, 2023.
- [13] I. Bica, A. Ilić, M. Bauer, G. Erdogan, M. Bošnjak, C. Kaplanis, A. A. Gritsenko, M. Minderer, C. Blundell, R. Pascanu *et al.*, "Improving fine-grained understanding in image-text pre-training," *arXiv preprint arXiv:2401.09865*, 2024.
- [14] Y. Pang, X. Zhao, T.-Z. Xiang, L. Zhang, and H. Lu, "Zoom in and out: A mixed-scale triplet network for camouflaged object detection," in *CVPR*, June 2022, pp. 2160–2170.
- [15] Z. Huang, H. Dai, T.-Z. Xiang, S. Wang, H.-X. Chen, J. Qin, and H. Xiong, "Feature shrinkage pyramid for camouflaged object detection with transformers," in *CVPR*, June 2023, pp. 5557–5566.
- [16] Q. Jia, S. Yao, Y. Liu, X. Fan, R. Liu, and Z. Luo, "Segment, magnify and reiterate: Detecting camouflaged objects the hard way," in *CVPR*, June 2022, pp. 4713–4722.
- [17] Y. Sun, S. Wang, C. Chen, and T.-Z. Xiang, "Boundary-guided camouflaged object detection," in *IJCAI*, 2022, pp. 1335–1341.
- [18] C. He, K. Li, Y. Zhang, L. Tang, Y. Zhang, Z. Guo, and X. Li, "Camouflaged object detection with feature decomposition and edge reconstruction," in *CVPR*, June 2023, pp. 22 046–22 055.
- [19] Z. Wu, D. P. Paudel, D.-P. Fan, J. Wang, S. Wang, C. Démonceaux, R. Timofte, and L. Van Gool, "Source-free depth for object pop-out," in *ICCV*, 2023.
- [20] Y. Pang, X. Zhao, T.-Z. Xiang, L. Zhang, and H. Lu, "Zoomnext: A unified collaborative pyramid network for camouflaged object detection," *IEEE Transactions on Pattern Analysis and Machine Intelligence*, 2024.
- [21] Z. Chen, R. Gao, T.-Z. Xiang, and F. Lin, "Diffusion model for camouflaged object detection," in *ECAI*, 2023.
- [22] D.-P. Fan, G.-P. Ji, P. Xu, M.-M. Cheng, C. Sakaridis, and L. Van Gool, "Advances in deep concealed scene understanding," *Visual Intelligence*, vol. 1, no. 1, p. 16, 2023.
- [23] C. H. Lampert, H. Nickisch, and S. Harmeling, "Learning to detect unseen object classes by between-class attribute transfer," in *CVPR*, 2009, pp. 951–958.
- [24] M. Cherti, R. Beaumont, R. Wightman, M. Wortsman, G. Ilharco, C. Gordon, C. Schuhmann, L. Schmidt, and J. Jitsev, "Reproducible scaling laws for contrastive language-image learning," in *CVPR*, June 2023, pp. 2818–2829.
- [25] G.-P. Ji, D.-P. Fan, P. Xu, M.-M. Cheng, B. Zhou, and L. Van Gool, "Sam struggles in concealed scenes—empirical study on" segment anything",*" Science China Information Sciences*, vol. 66, no. 226101, 2023.
- [26] Z. Tu, Y. Ma, Z. Li, C. Li, J. Xu, and Y. Liu, "Rgbt salient object detection: A large-scale dataset and benchmark," *IEEE TMM*, vol. 25, pp. 4163–4176, 2023.
- [27] Q. Zhang, N. Huang, L. Yao, D. Zhang, C. Shan, and J. Han, "Rgb-t salient object detection via fusing multi-level cnn features," *IEEE TIP*, vol. 29, pp. 3321–3335, 2020.
- [28] Z. Chen, R. Cong, Q. Xu, and Q. Huang, "Dpanet: Depth potentiality-aware gated attention network for rgb-d salient object detection," *IEEE TIP*, vol. 30, pp. 7012–7024, 2021.
- [29] J.-X. Zhao, Y. Cao, D.-P. Fan, M.-M. Cheng, X.-Y. Li, and L. Zhang, "Contrast prior and fluid pyramid integration for rgb-d salient object detection," in *CVPR*, June 2019.
- [30] N. Liu, N. Zhang, L. Shao, and J. Han, "Learning selective mutual attention and contrast for rgb-d saliency detection," *IEEE TPAMI*, vol. 44, no. 12, pp. 9026–9042, 2022.
- [31] Z. WU, D. P. Paudel, D.-P. Fan, J. Wang, S. Wang, C. Démonceaux, R. Timofte, and L. Van Gool, "Source-free depth for object pop-out," in *ICCV*, October 2023, pp. 1032–1042.
- [32] J. He, C. Zhou, X. Ma, T. Berg-Kirkpatrick, and G. Neubig, "Towards a unified view of parameter-efficient transfer learning," in *ICLR*, 2022.
- [33] N. Houlsby, A. Giurgiu, S. Jastrzebski, B. Morrone, Q. De Larousilhe, A. Gesmundo, M. Attariyan, and S. Gelly, "Parameter-efficient transfer learning for NLP," in *ICML*, vol. 97. PMLR, 2019, pp. 2790–2799.
- [34] J. Pfeiffer, A. Kamath, A. Rücklé, K. Cho, and I. Gurevych, "AdapterFusion: Non-destructive task composition for transfer learning," in *EACL*, 2021, pp. 487–503.
- [35] D. Yin, L. Hu, B. Li, and Y. Zhang, "Adapter is all you need for tuning visual tasks," *arXiv preprint arXiv:2311.15010*, 2023.
- [36] D. Yin, L. Hu, B. Li, Y. Zhang, and X. Yang, "5
- [37] S. Chen, C. GE, Z. Tong, J. Wang, Y. Song, J. Wang, and P. Luo, "Adaptformer: Adapting vision transformers for scalable visual recognition," in *NeurIPS*, vol. 35, 2022, pp. 16 664–16 678.
- [38] W. Liu, X. Shen, C.-M. Pun, and X. Cun, "Explicit visual prompting for low-level structure segmentations," in *CVPR*, June 2023, pp. 19 434–19 445.
- [39] W. Liu, X. Shen, C.-M. Pun, and X. Cun, "Explicit visual prompting for universal foreground segmentations," *arXiv preprint arXiv:2305.18476*, 2023.
- [40] T. Chen, L. Zhu, C. Deng, R. Cao, Y. Wang, S. Zhang, Z. Li, L. Sun, Y. Zang, and P. Mao, "Sam-adapter: Adapting segment anything in underperformed scenes," in *ICCVW*, 2023, pp. 3367–3375.
- [41] E. J. Hu, Y. Shen, P. Wallis, Z. Allen-Zhu, Y. Li, S. Wang, L. Wang, and W. Chen, "LoRA: Low-rank adaptation of large language models," in *ICLR*, 2022.
- [42] M. Jia, L. Tang, B.-C. Chen, C. Cardie, S. Belongie, B. Hariharan, and S.-N. Lim, "Visual prompt tuning," in *ECCV*, 2022, pp. 709–727.
- [43] E. B. Zaken, S. Ravfogel, and Y. Goldberg, "Bitfit: Simple parameter-efficient fine-tuning for transformer-based masked language-models," *arXiv preprint arXiv:2106.10199*, 2022.
- [44] Y. Fang, Q. Sun, X. Wang, T. Huang, X. Wang, and Y. Cao, "Eva-02: A visual representation for neon genesis," *arXiv preprint arXiv:2303.11331*, 2023.
- [45] Y. Fang, W. Wang, B. Xie, Q. Sun, L. Wu, X. Wang, T. Huang, X. Wang, and Y. Cao, "Eva: Exploring the limits of masked visual representation learning at scale," in *CVPR*, June 2023, pp. 19 358–19 369.
- [46] X. Glorot, A. Bordes, and Y. Bengio, "Deep sparse rectifier neural networks," in *Proceedings of the fourteenth international conference on artificial intelligence and statistics. JMLR Workshop and Conference Proceedings*, 2011, pp. 315–323.
- [47] Y. Li, H. Mao, R. Girshick, and K. He, "Exploring plain vision transformer backbones for object detection," in *Computer Vision – ECCV 2022*, S. Avidan, G. Brostow, M. Cissé, G. M. Farinella, and T. Hassner, Eds. Cham: Springer Nature Switzerland, 2022, pp. 280–296.
- [48] L. Wang, H. Lu, Y. Wang, M. Feng, D. Wang, B. Yin, and X. Ruan, "Learning to detect salient objects with image-level supervision," in *CVPR*, 2017.
- [49] T.-N. Le, T. V. Nguyen, Z. Nie, M.-T. Tran, and A. Sugimoto, "Anabranh network for camouflaged object segmentation," *CVIU*, vol. 184, pp. 45–56, 2019.
- [50] P. Skurowski, H. Abdulameer, J. Błaszczyk, T. Depta, A. Kornacki, and P. Koziół, "Animal camouflage analysis: Chameleon database," *Unpublished manuscript*, vol. 2, no. 6, p. 7, 2018.
- [51] J. Li, D. Li, S. Savarese, and S. Hoi, "BLIP-2: bootstrapping language-image pre-training with frozen image encoders and large language models," in *ICML*, 2023.
- [52] T. Dao, D. Fu, S. Ermon, A. Rudra, and C. Ré, "Flashattention: Fast and memory-efficient exact attention with io-awareness," *Advances in Neural Information Processing Systems*, vol. 35, pp. 16 344–16 359, 2022.
- [53] I. Loshchilov and F. Hutter, "Decoupled weight decay regularization," *arXiv preprint arXiv:1711.05101*, 2017.
- [54] R. Margolin, L. Zelnik-Manor, and A. Tal, "How to evaluate foreground maps?" in *CVPR*, 2014, pp. 248–255.
- [55] M.-M. Cheng and D.-P. Fan, "Structure-measure: A new way to evaluate foreground maps," *IJCV*, vol. 129, no. 9, pp. 2622–2638, 2021.
- [56] D.-P. Fan, M.-M. Cheng, Y. Liu, T. Li, and A. Borji, "Structure-measure: A new way to evaluate foreground maps," in *ICCV*, 2017.
- [57] D.-P. Fan, C. Gong, Y. Cao, B. Ren, M.-M. Cheng, and A. Borji, "Enhanced-alignment measure for binary foreground map evaluation," in *IJCAI*. AAAI Press, 2018.
- [58] N. Liu, N. Zhang, K. Wan, L. Shao, and J. Han, "Visual saliency transformer," in *ICCV*, October 2021, pp. 4722–4732.
- [59] E. Xie, W. Wang, Z. Yu, A. Anandkumar, J. M. Alvarez, and P. Luo, "Segformer: Simple and efficient design for semantic segmentation with transformers," in *NeurIPS*, vol. 34, 2021, pp. 12 077–12 090.
- [60] S. Yu, B. Zhang, J. Xiao, and E. G. Lim, "Structure-consistent weakly supervised salient object detection with local saliency coherence," in *AAAI*, vol. 35, no. 4, 2021, pp. 3234–3242.
- [61] Z. Liang, T. Wang, X. Zhang, J. Sun, and J. Shen, "Tree energy loss: Towards sparsely annotated semantic segmentation," in *CVPR*, 2022, pp. 16 907–16 916.
- [62] N. Ravi, V. Gabeur, Y.-T. Hu, R. Hu, C. Ryali, T. Ma, H. Khedr, R. Rädle, C. Rolland, L. Gustafson, E. Mintun, J. Pan, K. V. Alwala, N. Carion, C.-Y. Wu, R. Girshick, P. Dollár, and C. Feichtenhofer, "Sam 2: Segment anything in images and

- videos," *arXiv preprint arXiv:2408.00714*, 2024. [Online]. Available: <https://arxiv.org/abs/2408.00714>
- [63] L. Tang and B. Li, "Evaluating sam2's role in camouflaged object detection: From sam to sam2," *arXiv preprint arXiv:2407.21596*, 2024.
 - [64] J. Pei, T. Cheng, D.-P. Fan, H. Tang, C. Chen, and L. Van Gool, "Osformer: One-stage camouflaged instance segmentation with transformers," in *ECCV*. Springer, 2022.
 - [65] X. Hu, S. Wang, X. Qin, H. Dai, W. Ren, D. Luo, Y. Tai, and L. Shao, "High-resolution iterative feedback network for camouflaged object detection," in *AAAI*, 2023, pp. 881–889.
 - [66] X. Li, J. Yang, S. Li, J. Lei, J. Zhang, and D. Chen, "Locate, refine and restore: A progressive enhancement network for camouflaged object detection," in *IJCAI*, 2023, pp. 1116–1124.
 - [67] Q. Wang, J. Yang, X. Yu, F. Wang, P. Chen, and F. Zheng, "Depth-aided camouflaged object detection," in *ACMMM*, 2023, pp. 3297–3306.
 - [68] M. Geva, R. Schuster, J. Berant, and O. Levy, "Transformer feed-forward layers are key-value memories," *arXiv preprint arXiv:2012.14913*, 2020.
 - [69] Y. Li, H. Wang, Y. Duan, and X. Li, "Clip surgery for better explainability with enhancement in open-vocabulary tasks," *arXiv preprint arXiv:2304.05653*, 2023.
 - [70] O. Ronneberger, P. Fischer, and T. Brox, "U-net: Convolutional networks for biomedical image segmentation," in *Medical image computing and computer-assisted intervention—MICCAI 2015: 18th international conference, Munich, Germany, October 5–9, 2015, proceedings, part III* 18. Springer, 2015, pp. 234–241.
 - [71] D.-P. Fan, G.-P. Ji, T. Zhou, G. Chen, H. Fu, J. Shen, and L. Shao, "Pranet: Parallel reverse attention network for polyp segmentation," in *International conference on medical image computing and computer-assisted intervention*. Springer, 2020, pp. 263–273.
 - [72] D. Jha, P. H. Smedsrud, M. A. Riegler, P. Halvorsen, T. De Lange, D. Johansen, and H. D. Johansen, "Kvasir-seg: A segmented polyp dataset," in *MultiMedia modeling: 26th international conference, MMM 2020, Daejeon, South Korea, January 5–8, 2020, proceedings, part II* 26. Springer, 2020, pp. 451–462.
 - [73] J. Silva, A. Histace, O. Romain, X. Dray, and B. Granado, "Toward embedded detection of polyps in wce images for early diagnosis of colorectal cancer," *International journal of computer assisted radiology and surgery*, vol. 9, pp. 283–293, 2014.